# Flow-Permeable and Tunable Metalens for Subdiffraction Waterborne-Sound Focusing

Lijuan Fan and Jun Mei*
*School of Physics, South China University of Technology, Guangzhou 510640, China*

(Received 24 September 2022; revised 26 November 2022; accepted 23 December 2022; published 9 February 2023)

Metalenses with high-efficiency focusing functionality and a water-flow-permeable structure are desired in various acoustic applications, such as medical imaging and underwater navigation. Here, we propose a design paradigm for a metalens for waterborne sound with a compact and simple configuration. The metalens is composed of an open central region reserved as a steady water-flow channel, and a metagrating-based peripheral region consisting of a grating of meta-atoms. Each meta-atom containing two elliptical iron cylinders is smartly designed according to the grating diffraction theory and intelligent optimization algorithm, so that it can deflect a normally incident wave along the desired direction toward the focal spot. In this way, subdiffraction focusing with a high energy concentration ratio is achieved, which breaks the conventional Rayleigh-Abbe diffraction limit in the focal plane. Here the subdiffraction focusing is due to the coherent interference in the far field of the ±first-order diffracted waves from each meta-atom, and is attributed to the superoscillation phenomenon. Interestingly, the focal depth of the metalens can be conveniently tuned by applying a background water flow with different velocities and directions, and the superresolution focusing effect is sustained regardless of whether there is a water flow or not. Since the magnitude and direction of the water-flow velocity can be electrically controlled, the compact and open configuration of the metalens not only provides a flexible and practical solution for sharp and controllable sound focusing, but also has potential applications in metagrating-based planar acoustic devices.

DOI: 10.1103/PhysRevApplied.19.024026

## I. INTRODUCTION

Conventional refractive components control the wave front of an incoming wave through the gradually accumulated phase change along its propagation path. Thus, they are usually bulky, costly, and time consuming to manufacture. In recent years, the metalens has emerged as a versatile and compact platform for wave-front shaping and focusing, where the phase is accurately controlled by subwavelength-spaced meta-atoms with thicknesses at the wavelength scale or below [1,2]. Such a flat configuration or miniaturized thickness leads to compact and high-efficiency wave-manipulating elements, exhibiting the desired performance for future applications such as portable and wearable devices. Differing from optical metalenses, many applications of acoustic metalenses call for the shaping or focusing of sound waves in a flowing fluid, because the background flows (airflow or water flow) must have a free channel for the proper functioning of the corresponding devices. Thus, a fluid flow passage and sharp sound focusing are simultaneously demanded, which require the existence of an airflow or water-flow channel in the design of the metalens.

In recent years, metamaterials with holes have been designed to efficiently *block* sound waves, where the holes enable airflow for ventilation [3–8]. Such flow-permeable metamaterials are desired in applications such as an “ideal” meeting room with concurrent sound insulation and fresh air circulation. Although simultaneous sound insulation and air ventilation were demonstrated in these works, it is still challenging to realize sharp sound focusing in a fluid-flow-filled environment. Maybe one of the reasons is that people intuitively think fluid flow is in contrast with high-efficiency wave focusing. Conventional methods of sound focusing rely on deflecting all incident wave energy toward the same focal spot, thus it is natural to avoid the use of open structures so that as much wave energy as possible can be collected and redirected toward the focus. Such an intuition does not suggest an open channel in the structure of a metalens. However, fluid flow is indispensable in many situations, especially in underwater acoustics where the water flow is not only ambient but also necessary for heat dissipation. Obviously, there is an intrinsic trade-off between the efficiencies of sound-wave focusing and fluid flow, because a stronger flow passage (which requires a large open area ratio) generally implies a poorer focusing performance. Therefore, designing a sharp focusing yet flow-permeable metalens remains a challenge.

---

*phjunmei@scut.edu.cn

In this article, we show that high-efficiency waterborne-sound focusing can be realized in a steady water flow by utilizing a different design paradigm for the metalens. To this end, we divide the metalens into two regions: a central open region allowing a free water flow, and a metagrating-based peripheral region redirecting the incoming waves to the focal spot. We note that a metagrating, instead of a metasurface [9–22], is used here for the peripheral region of the metalens, simply because the diffraction efficiency for a gradient metasurface is often low for large steering angles [10]. In contrast, a metagrating can sustain a close-to-unity manipulation efficiency even for a steep diffraction angle, which is beneficial to a metalens with a high numerical aperture (NA). Furthermore, the size of the meta-atoms in a metagrating is of the same order of magnitude as the working wavelength, which is easy to scale down for higher working frequencies. The meta-atoms in a metasurface, in comparison, are usually in the subwavelength scale so that a fast-varying phase or impedance profile can be adequately discretized and implemented; therefore, they are more challenging to fabricate for a small working wavelength. In recent years, metagratings have been used in various wave-manipulation scenarios including anomalous reflection or refraction [23–29], nonreciprocal transmission [30], multifunctional devices [31], cloaking [32], sound vortices [33], elastic wave manipulation [34,35], and far-field focusing [36–40]. However, the realization of wave-focusing functionality in a steady fluid-flow environment is still an open question, although there is high demand for this in many underwater acoustic applications.

To overcome this difficulty, we marry the rising concept of the metagrating with the principle of the metalens and propose an alternative design paradigm for the metalens. We utilize the high-diffraction-efficiency characteristics of metagratings to realize subdiffraction focusing. By exploiting the diffraction contribution from the peripheral region of the metalens, we intentionally bring the diffracted wave components carrying high transverse wave vectors ($k_{\|}$) to the focal spot with a high efficiency. Interestingly, such a compact and open design paradigm not only allows for a subdiffraction focusing of waterborne sound that breaks the Rayleigh-Abbe diffraction limit of 0.5λ/NA, but also permits the steady and consecutive flow of water in the central region of the metalens, compatible with the flow-permeable application scenarios. Furthermore, the focusing functionality of the metalens can be tuned in a convenient way by controlling the applied water-flow velocity. We find that the focal length can be tuned by applying water flows with different velocities, and a sharp focusing effect still holds even when the direction of the water flow is reversed. Since the magnitude and direction of the water-flow velocity can be electrically controlled, our metalens design provides a flexible and practical solution for different application scenarios such as medical imaging and underwater navigation.

## II. DESIGN METHOD BASED ON BRAGG'S DIFFRACTION THEORY AND OPTIMIZATION ALGORITHM

To achieve the desired focusing effect, we start with the right half of the metalens, which is composed of a one-dimensional (1D) array of meta-atoms, as shown schematically in Fig. 1(a). Each meta-atom (i.e., unit cell of the metagrating) consists of two elliptical iron cylinders, whose geometric parameters include the major semiaxes $a_1$ and $a_2$, minor semiaxes $b_1$ and $b_2$, rotation angles $\varphi_1$ and $\varphi_2$, and their center positions $(x_1, 0)$ and $(x_2, y_2)$, as shown in the inset. For the iron cylinders, their mass density, longitudinal velocity, and transverse velocity are $\rho_1 = 7670\ \mathrm{kg/m^3}$, $c_p = 6010\ \mathrm{m/s}$, and $c_s = 3230\ \mathrm{m/s}$, respectively. The metalens works for waterborne sound, so the background material is water, with a mass density $\rho = 1000\ \mathrm{kg/m^3}$ and sound velocity $c_0 = 1490$ m/s. Each meta-atom is individually designed such that it deflects the normally incident plane wave ($p_{\mathrm{in}}$) along the specific diffraction angle $\theta_L$ ($L = 1, 2, \ldots$) toward the focal spot. Although the metalens design is based on a two-dimensional (2D) diffraction analysis, it is easy to extend it by rotating the meta-atoms around the $y$ axis to obtain a full three-dimensional (3D) metalens, as shown in Fig. 1(b).

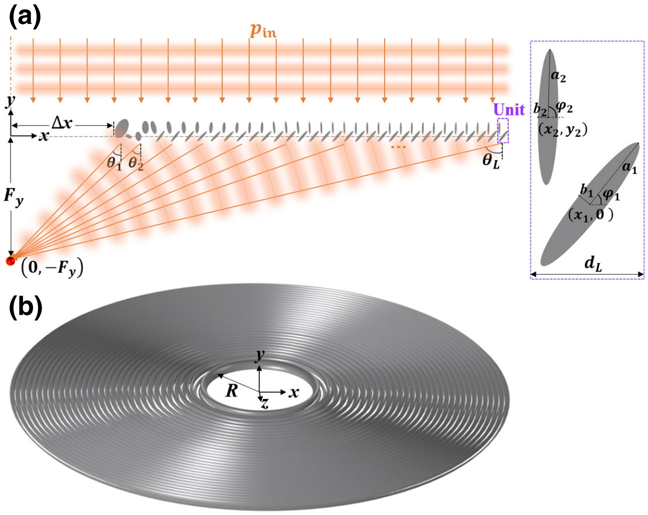

FIG. 1. Schematic of the metalens. (a) 2D cross-section view of the metalens where only the right half is shown. The metalens is composed of 32 meta-atoms, with each meta-atom consisting of two elliptical iron cylinders, and the geometrical parameters are marked in the inset. The focusing functionality is achieved when each meta-atom deflects the normally incident plane wave along the desired direction toward the same focal spot. (b) 3D full metalens is obtained by rotating the 2D cross section around the $y$ axis.

When a plane wave is normally incident on a grating, the reflected and refracted waves propagate along several discrete diffraction directions according to the grating diffraction theory. The reflective and refractive angles are determined by the Bragg diffraction condition, i.e., $d\sin\theta^{(n)} = n\lambda$, where $\theta^{(n)}$ represents the diffraction angle for the $n$th-order reflected or refracted wave, and $\lambda$ is the wavelength in water. As shown in Fig. 1(a), we let the negative first-order ($n = -1$) refracted wave of each meta-atom converge to the focal spot $(0,-F_y)$. To this end, the $L$th ($L = 1, 2, \ldots$) meta-atom needs to satisfy the following diffraction condition and geometric relationship:

$$d_L = -\lambda/\sin\theta_L^{(-1)}, \tag{1}$$

$$\tan\left|\theta_L^{(-1)}\right| = \left(\Delta x + \sum_{i=1,\ldots,L} d_i - d_L/2\right)\Bigg/ F_y, \tag{2}$$

where $d_L$ and $\theta_L^{(-1)}$ represent grating period and negative first-order refractive angle of the $L$th meta-atom, respectively. To be more specific, we assume that the working wavelength is $\lambda = 7.45$ mm (corresponding to a working frequency of 200 kHz) and a focal length of $F_y = 15\lambda$. According to Eq. (1), the grating period of the first meta-atom is $d_1 = 14.06$ mm at the diffraction angle $\theta_1^{(-1)} = -32^\circ$. From $\theta_1^{(-1)}$ and Eq. (2) we obtain $\Delta x = 8.43\lambda$, which is the distance from the first meta-atom to the $y$ axis (i.e., the axis of the metalens). For a given focal length $F_y$ and the first meta-atom's diffraction angle $\theta_1^{(-1)}$, the grating period $d_L$ and diffraction angle $\theta_L^{(-1)}$ of the other meta-atoms ($L = 2, 3 \ldots$) can be uniquely determined in sequence. The metalens is composed of 32 meta-atoms that feature a high NA, with the diffraction angles covering a wide range from $-32^\circ$ to $-72.1^\circ$. Here the distance $\Delta x = 8.43\lambda$ is chosen so that the metalens has a large open area in the central region, which is important since a wide channel needs to be reserved for free water flow.

The reason why the diffraction angle for the first meta-atom is chosen as $|\theta_1^{(-1)}| = 32^\circ$ is based on the following considerations. On one hand, since $\sin|\theta_1^{(-1)}| > 1/2$, according to the Bragg diffraction condition, only six diffraction orders (three reflected orders plus three refracted orders for $n = 0, \pm 1$) are propagating waves, and all higher orders ($|n| \geq 2$) are evanescent waves. Therefore, we only need to control six diffraction orders to achieve the desired focusing functionality implemented by the negative first-order ($n = -1$) refracted wave. In comparison, if we choose a smaller diffraction angle with $|\theta_1^{(-1)}| < 30^\circ$ and $\sin|\theta_1^{(-1)}| < 1/2$, we have to simultaneously control at least ten diffraction orders (five reflected and five refracted orders with $n = 0, \pm 1, \pm 2$) to achieve the desired focusing functionality, which inevitably leads to a much more complicated configuration of the first meta-atom. We aim to use a metalens with as simple a structure as possible, which is beneficial to sample fabrication and potential applications. Thus, a diffraction angle $|\theta_1^{(-1)}|$ larger than 30° is preferred. On the other hand, we want to keep the central open area of the metalens relatively large to accommodate a high-efficiency water-flow channel, and it turns out that $\theta_1^{(-1)} = -32^\circ$ is appropriate for the first meta-atom.

In the design of the metalens, the degrees of freedom (DOF) of meta-atoms are the geometrical parameters of the two elliptical cylinders, including $a_1$, $a_2$, $b_1$, $b_2$, $\varphi_1$, $\varphi_2$, $x_1$, $x_2$, and $y_2$. We need to intelligently determine these parameters to realize the desired focusing functionality: the diffracted wave propagates only along the $n = -1$ channel, and all other diffraction orders (including all reflected diffraction orders and the $n = 0, +1$ refracted diffraction orders) are completely suppressed. To meet this requirement, we utilize an intelligent optimization algorithm based on the combination of a global optimization algorithm and a local optimization algorithm.

To be more specific, we use optimization algorithms in two steps. In the first step, we use the genetic algorithm (GA) *or* particle swarm optimization (PSO) to perform a global search. The GA is an evolutionary algorithm simulating the crossover and mutation of chromosome genes in the process of biological evolution to search for the optimal solution. PSO solves a problem by having a population of candidate solutions (i.e., particles) and moving these particles around in the search space according to simple mathematical formulae over a particle's position and velocity, and it can search very large spaces of candidate solutions. Either the GA or PSO can be used to locate the global minimum in the parameter space.

In the second step, we use the pattern search algorithm to perform a refined local search around the global minimum found in the first step. To be more specific, we use the Nelder-Mead algorithm to search for a better solution than the current one in each iteration. The Nelder-Mead algorithm is a numerical method used to find the minimum or maximum of an objective function in a multidimensional space. It is a direct search method and is often applied to nonlinear optimization problems for which derivatives may not be known. With such a two-step optimization scheme, we can find improved solutions with further enhanced diffraction efficiency for each meta-atom in the lens.

When applying the intelligent optimization algorithm, the geometrical parameters ($a_1$, $a_2$, $b_1$, $b_2$, $\varphi_1$, $\varphi_2$, $x_1$, $x_2$, and $y_2$) of each meta-atom are the optimization variables, and the efficiency of the desired diffraction channel (i.e., $T_{-1} \to 100\%$) is the optimization objective. At this stage of design, no water flow is involved. We use the pressure acoustics (frequency domain) and solid mechanics module with an acoustic-solid interaction interface in COMSOL Multiphysics for the full-wave numerical simulations,

TABLE I. Optimized geometrical parameters of the 32 meta-atoms.

| Unit no. | $L$ | $\lvert\theta_L^{(-1)}\rvert$ (deg) | $d_L$(mm) |
|---|---|---|---|
| 1 | 1 | 32 | 14.06 |
| 2 | 2 | 36.6 | 12.50 |
| 3 | 3 | 40.4 | 11.49 |
| 4 | 4 | 43.6 | 10.80 |
| 5 | 5 | 46.3 | 10.30 |
| 6 | 6 | 48.7 | 9.92 |
| 7 | 7 | 50.8 | 9.61 |
| 8 | 8, 9 | 52.7, 54.4 | 9.37, 9.16 |
| 9 | 10, 11 | 55.9, 57.3 | 9.00, 8.85 |
| 10 | 12 to 14 | 58.6, 59.8, 60.9 | 8.73, 8.62, 8.53 |
| 11 | 15 to 18 | 61.9, 62.8, 63.7, 64.5 | 8.45, 8.38, 8.31, 8.25 |
| 12 | 19 to 23 | 65.3, 66, 66.7, 67.3, 67.9 | 8.20, 8.16, 8.11, 8.08, 8.04 |
| 13 | 24 to 32 | 68.5, 69, 69.5, 70, 70.5, 70.9, 71.3, 71.7, 72.1 | 8.01, 7.98, 7.95, 7.93, 7.90, 7.88, 7.87, 7.85, 7.83 |

| Unit no. | $a_1$ (mm) | $b_1$ (mm) | $\varphi_1$ (deg) | $(x_1, y_1)$ (mm) | $a_2$ (mm) | $b_2$ (mm) | $\varphi_2$ (deg) | $(x_2, y_2)$ (mm) |
|---|---|---|---|---|---|---|---|---|
| 1 | 2.272 | 1.196 | 152.9 | (11.21, 0) | 7.430 | 4.200 | 63.3 | (6.222, 5.674) |
| 2 | 3.328 | 2.068 | 98.5 | (4.142, 0) | 4.625 | 2.455 | 91.9 | (9.288, 6.555) |
| 3 | 5.057 | 0.857 | 54.0 | (7.667, 0) | 4.767 | 1.841 | 105.2 | (2.733, 6.474) |
| 4 | 5.036 | 0.842 | 51.5 | (6.959, 0) | 4.540 | 1.627 | 100.1 | (2.419, 6.477) |
| 5 | 5.008 | 0.829 | 50.2 | (6.405, 0) | 4.358 | 1.472 | 93.9 | (2.214, 6.331) |
| 6 | 5.066 | 0.848 | 45.5 | (5.201, 0) | 4.178 | 1.321 | 86.9 | (1.696, 6.394) |
| 7 | 5.053 | 0.842 | 45.7 | (5.178, 0) | 4.057 | 1.223 | 85.1 | (1.760, 6.321) |
| 8 | 5.064 | 0.846 | 46.1 | (4.956, 0) | 3.926 | 1.108 | 86.2 | (1.562, 6.255) |
| 9 | 5.119 | 0.867 | 45.9 | (4.795, 0) | 4.145 | 0.924 | 87.1 | (1.543, 6.265) |
| 10 | 5.142 | 0.896 | 49.3 | (4.800, 0) | 4.570 | 0.800 | 94.8 | (1.444, 6.385) |
| 11 | 5.142 | 0.899 | 49.8 | (4.530, 0) | 4.389 | 0.650 | 91.9 | (1.325, 6.173) |
| 12 | 5.162 | 0.917 | 49.8 | (4.372, 0) | 4.457 | 0.663 | 90.4 | (1.466, 5.729) |
| 13 | 5.166 | 0.928 | 51.6 | (4.141, 0) | 4.481 | 0.665 | 88.4 | (1.356, 5.758) |

where both longitudinal and transverse wave modes in iron cylinders are rigorously taken into consideration. With the help of the intelligent optimization algorithm, the optimized geometric parameters of all 32 meta-atoms can be quickly obtained, and they are listed in Table I.

Since each meta-atom deflects the normally incident plane wave along a different direction toward the same focal spot, it is reasonable to expect that the geometrical parameters of each meta-atom may vary from the inner to the outer parts of the metalens. In fact, there are 13 sets of optimized geometric parameters for the 32 meta-atoms. The first seven rows in Table I correspond to cases where the diffraction angle $\theta_L^{(-1)}$ is relatively small, i.e., $32^\circ \le |\theta_L^{(-1)}| \le 50.8^\circ$, so that each set of geometrical parameters works for only one meta-atom that deflects the incident wave along one diffraction angle. For the last six rows in Table I, the refraction angle $|\theta_L^{(-1)}|$ is relatively large, and different meta-atoms with different diffraction angles may share the same set of geometrical parameters by simply tuning the grating period $d_L$. Take the eighth row in Table I as an example, the eighth and ninth meta-atoms need to deflect the incident wave along the directions of $\theta_8^{(-1)} = -52.7^\circ$ and $\theta_9^{(-1)} = -54.4^\circ$, respectively. Such requirements can be met by using the same set of parameters (as explicitly listed in the eighth row) by setting $d_8 = 9.37$ mm and $d_9 = 9.16$ mm, respectively, according to $d_L = -\lambda / \sin \theta_L^{(-1)}$. In a similar way, each parameter set in the 9th–13th rows are suitable for more than one meta-atom and can be used to deflect the incident wave along different diffraction angles. In this way, the design process of the metalens can be greatly simplified. Finally, we obtain a simply structured metalens consisting of 32 meta-atoms, for which only 13 sets of geometric parameters are used.

Then we assemble these 32 meta-atoms into the right half of the metalens, as shown in Fig. 1(a). The focus position of $F_y = 15\lambda$ and $\Delta x = 10.16\lambda$ (relative to the first meta-atom) is obtained by full-wave numerical simulation of the right half of the lens, which is slightly shifted from the design target of $F_y = 15\lambda$ and $\Delta x = 8.43\lambda$. This shift is not unexpected, because the theoretical formulae [Eqs. (1) and (2)] are based on the grating diffraction theory where each meta-atom is arranged in an infinitely long 1D array with the same period $d$. However, in an actual metalens each meta-atom is in a finite array with its period $d_L$ varying from one atom to another. Another reason for the shift is that the metalens is open (containing no meta-atoms) in the central region where $r < \Delta x$, so that there is no diffraction contribution to the focusing when $|\theta_L^{(-1)}| < 32^\circ$.

By rotating the right half of the lens around the $y$ axis, we finally obtain a 3D metalens with a high numerical aperture $\mathrm{NA} = \sin(72.1^\circ) = 0.952$ and a rather high open area ratio of 26.5%. The sound-focusing effect of the metalens is then simulated and studied. In the left panels of Fig. 2(a) we plot the intensity distribution of the total pressure field $|p|^2$ in the longitudinal $x$-$y$ plane and the transverse $x$-$z$ plane (both of which go through the focal spot). A sharp focusing effect is obtained. The intensity profiles along the $y$ axis (i.e., the axis of the metalens) is plotted in Fig. 2(b) as a red curve, where a highly concentrated energy distribution around the focal spot is observed. The maximum pressure intensity is above 9000 Pa$^2$, with the intensity of the incident plane wave being 1 Pa$^2$.

More interesting results are seen in Fig. 2(c), where the pressure intensity profile along the $x$ axis in the focal plane is plotted as a red curve, exhibiting a subdiffraction feature. We note that subdiffraction is defined as describing any optical or acoustic device or process involving a dimension shorter than that of the diffraction limit of the light or sound wave involved. It is well known that, due to the diffraction effect, the resolution of conventional optics is limited by the Rayleigh-Abbe diffraction limit of $0.5\lambda/\mathrm{NA}$. That is to say, in conventional optics and acoustics the full width at half maximum (FWHM) of the wave intensity in the focal plane is usually larger than $0.5\lambda/\mathrm{NA}$. In contrast, if a FWHM smaller than this limit ($0.5\lambda/\mathrm{NA}$) is realized in the focal plane, we call it subdiffraction focusing. In Fig. 2(c), the FWHM is $0.409\lambda$, which is smaller than the Rayleigh-Abbe diffraction limit of $0.5\lambda/\mathrm{NA} = 0.525\lambda$, thus implying subdiffraction focusing.

This subdiffraction focusing effect is due to the mathematical fact that a band-limited function in the focal plane can oscillate arbitrarily faster than the highest transverse Fourier components ($k_{\parallel,\max}$) it contains, a phenomenon called superoscillation [41–43]. In recent years, there has been growing interest in seeking far-field superresolution devices that break the traditional Rayleigh-Abbe diffraction limit of $0.5\lambda/\mathrm{NA}$ [39,44–49]. In our study, the subdiffraction focusing of waterborne sound is achieved in the far-field region with a focal length of $F_y = 15\lambda$. At this distance, all higher order ($|n| \geq 2$) diffracted waves are evanescent modes decaying to zero rapidly, and the only contribution comes from the negative (positive) first-order waves diffracted by the meta-atoms in the right-half (left-half) lens. It is their coherent interference in the far-field region that leads to the formation of subdiffraction focusing. Furthermore, the wave diffracted by the meta-atoms in the peripheral region of the metalens has a larger diffraction angle $|\theta_L^{(-1)}|$ and thus carries a larger transverse wave-vector component $k_\parallel = k_0 \sin\theta_L^{(-1)}$ compared with the meta-atoms in the central region. Since a large $k_\parallel$ component means a higher transverse resolution in the focusing plane, it is natural to infer that the

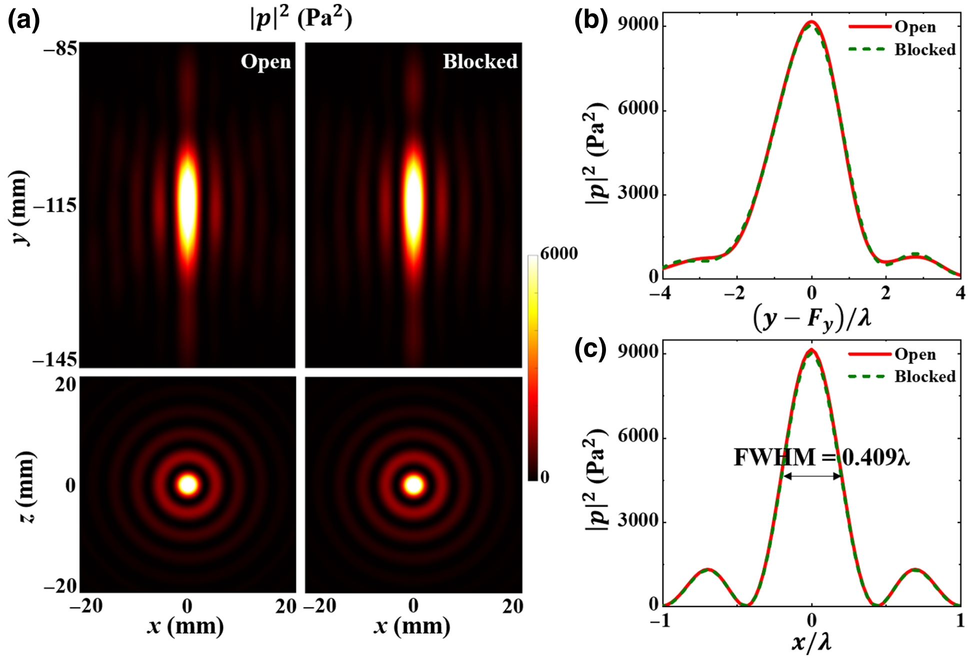

FIG. 2. Focusing effect when the central region of the metalens is blocked. (a) Pressure intensity $|p|^2$ distributions in the longitudinal propagation plane (upper panel) and the transverse focal plane (lower panel). Left and right panels correspond to the central region being open and blocked, respectively. (b),(c) Intensity profiles along the $y$ axis (the axis of metalens) and the $x$ axis in the focal plane, respectively, and the corresponding FWHMs are marked in (c).

peripheral region contributes more substantially than the central region of the metalens in terms of subdiffraction focusing.

To verify our speculation, we intentionally block the central region of the 3D metalens by covering it with a sound-hard boundary sheet of radius $R = \Delta x$. The corresponding pressure intensity field $|p|^2$ is plotted in the right panel of Fig. 2(a). Nearly no difference can be seen between the right and left panels, with the latter corresponding to the metalens of Fig. 1 (i.e., the original design with an open central region). The focal lengths ($F_y$) for the 3D metalens with open and blocked central regions are found to be 15.33λ and 15.36λ, respectively, which are slightly different from the design target of $F_y = 15\lambda$. The intensity profiles along the $y$ axis and along the $x$ axis in the focal plane are plotted in Figs. 2(b) and 2(c), respectively, and we observe that the results for the two cases (open versus blocked) are almost exactly the same. Interestingly, in both cases the FWHMs in the transverse focal plane are equal to 0.409λ.

## III. RESULTS

The results in the previous section show that a sharp focusing effect can be achieved even when the central region is blocked. Thus, it is natural to infer that the focusing functionality can still be achieved even when there is a free water flow through the central region of the metalens. In this section, we apply a steady water flow and study its influence on the focusing effect. When a water flow is introduced, we use the aeroacoustic module (based on the linearized Navier-Stokes equation) and solid mechanics module with an aeroacoustic-structure Multiphysics boundary in COMSOL for the full-wave numerical simulations. In this study, we consider a nonviscous water flow, and thus set the fluid viscosity (both dynamic viscosity and bulk viscosity), thermal conductivity, and viscous dissipation function to zero. After setting a nonzero background water flow field $\boldsymbol{v}_{\mathrm{bg}}$, we excite the metalens by a normally incident acoustic plane wave $p_{\mathrm{in}}$. The background flow velocity $\boldsymbol{v}_{\mathrm{bg}}$ is applied to the central open region of the metalens, which leads to a minimal influence on the previous optimization results without a water flow. As a demonstration, we introduce a nonuniform parabolic-shaped water-flow profile, i.e.,

$$\boldsymbol{v}_{\mathrm{bg}} = v_0 \left( -\frac{r^2}{R^2} + 1 \right) \hat{y}, \tag{3}$$

where $r$ is the distance to the axis of the metalens, and $v_0$ is the maximum flow velocity. The corresponding background flow field distribution is shown in Fig. 3(a), which clearly shows that the flow field exists only in the central region. A 2D cross-section view of the streamlines is shown in Fig. 3(b), where the flow velocity takes a maximum value in the center $r = 0$ and gradually drops to zero when $r \to R$. Such a parabolic-shaped flow profile is considered more realistic than a step-function-shape flow profile. In Fig. 3 the water flows in the $-y$ direction, therefore the maximum flow velocity is $-v_0$ and negative. Conversely, if the water flows in the $+y$ direction, the resulting maximum flow velocity would be $v_0$ and positive.

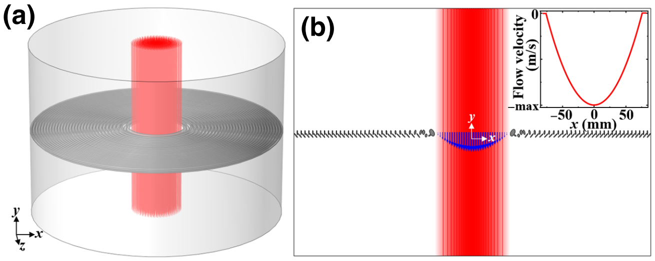

FIG. 3. Distribution of the background water-flow field. (a) Background water-flow velocity field $\boldsymbol{v}_{\mathrm{bg}}$ in 3D, where the red lines are the flow streamlines. (b) 2D cross-section view of (a), where the blue arrows indicate the direction of $\boldsymbol{v}_{\mathrm{bg}}$. In the inset, the water-flow velocity is plotted as a function of the transverse coordinate $x$.

We then impose different magnitudes of water flow velocity $v_0$, and study its influence on the focusing performance. For water flows in the $-y$ direction, we study three cases with $v_0 = -100$ m/s, $-50$ m/s, and $-20$ m/s, respectively. The corresponding intensity distributions $|p|^2$ in the $x$-$y$ plane are plotted in the left three panels of Fig. 4(a). Their focus positions ($-F_y$) are $-16.27\lambda$, $-15.76\lambda$, and $-15.55\lambda$, respectively. They are shifted from the original position $-F_y = -15.33\lambda$ (when there is no water flow) by a displacement of $-0.94\lambda$, $-0.43\lambda$, and $-0.22\lambda$, respectively. It is evident that the focal spot moves along the direction of the background flow velocity, and the moved distance is approximately proportional to the magnitude of the flow velocity $v_0$. To further verify this conjecture, we try another case by introducing a background flow field along the $+y$ direction, i.e., $v_0 = +50$ m/s. The corresponding intensity field distribution is shown in the rightmost panel of Fig. 4(a), giving a focus position of $-14.93\lambda$. In this case, the focal spot is moved from the original position by a displacement of 0.40λ, which is again along the direction of the background flow velocity, thus verifying our conjecture. For all cases, the intensity field distributions in the transverse focal plane are shown in Fig. 4(b), where highly concentrated wave energy focusing patterns are observed.

The intensity profiles along the $y$ axis and along the $x$ axis in the focal plane are shown in Figs. 4(c) and 4(d), respectively. Figure 4(c) clearly shows that the focus has a different extent of shift under the influence of different background flow velocities. Figure 4(d) shows that the FWHMs in the focal plane are 0.428λ, 0.419λ, 0.415λ,

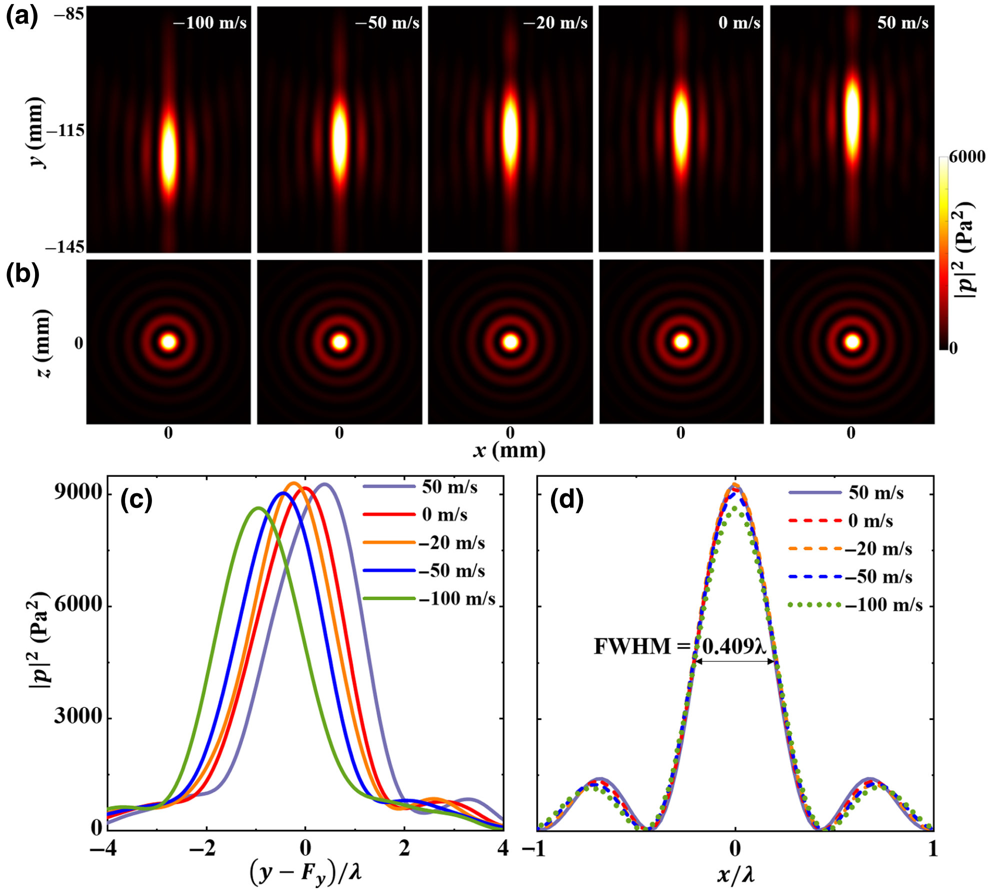

FIG. 4. Focusing effect of the metalens for different water-flow velocities. (a),(b) Intensity field distributions in the longitudinal propagation plane and in the transverse focal plane, respectively. Here the case of $v_0 = 0$ m/s corresponds to a metalens with an open central region but no water flow. (c),(d) Intensity profiles along the $y$ axis and the $x$ axis of the focal plane, respectively. The FWHM corresponding to $v_0 = 0$ m/s is marked in (d), and the FWHMs corresponding to other flow velocities have almost the same value.

and 0.400λ, respectively, for $v_0 = -100$ m/s, −50 m/s, −20 m/s, and +50 m/s.

The pressure field intensity peaks and FWHMs for different water flow velocities are summarized in Fig. 5. It is worth noting that the blue dashed line represents the conventional Rayleigh-Abbe diffraction limit of $0.5\lambda/\mathrm{NA} = 0.525\lambda$, and the orange dot-dashed line marks the superoscillation criterion of $0.38\lambda/\mathrm{NA} = 0.399\lambda$ [46]. The red squares always stay below the Rayleigh-Abbe limit, thus implying subdiffraction focusing by the metalens, regardless of whether there is a water flow or not. We also note that the red squares gradually approach the superoscillation criterion. When $v_0 = +50$ m/s, the FWHM is 0.400λ, which is very close to the criterion of 0.399λ. As shown by the gray triangles in Fig. 5, the peak intensity of the pressure is around 9000 Pa$^2$ for all cases, exhibiting a huge energy concentration effect at the focal spot.

These results can be summarized as follows. When the flow velocity is relatively large, e.g., $|v_0| > 20$ m/s, there is a substantial displacement of the focal spot along the water-flow direction, and the larger the water-flow velocity the more the position shift. We also study cases of slow water flow, and find when the flow velocity is small, e.g., $|v_0| < 10$ m/s, the position shift of the focal spot can be nearly neglected. However, the transverse resolution in the focal plane is almost constant, and it could stay below the Rayleigh-Abbe diffraction limit regardless of the magnitude and direction of the background water-flow velocity.

Furthermore, we also study the effect of viscosity on the focusing effect of the metalens. In the COMSOL Multiphysics simulation setup, we turn on the dynamic viscosity and bulk viscosity of the water flow, with their values being 0.001 Pa s and 0.0028 Pa s, respectively. Then we make two control simulations. The first one is performed when the background water-flow velocity is zero, i.e., $v_0 = 0$ m/s. In the second simulation, the background water-flow velocity is set as $v_0 = -20$ m/s. Both results show that the pressure intensity profiles $|p|^2$ along the $y$ axis and along the $x$ axis in the focal plane are only slightly affected compared with the results for the nonviscous case. Thus, we may conclude that the viscosity of the water flow

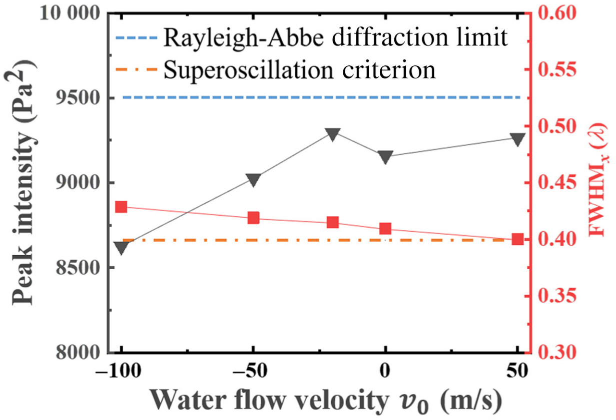

FIG. 5. Peak intensity (gray triangles) and FWHM$_x$ (red squares) in the focal plane of the metalens for five different water-flow velocities, i.e., $v_0 = -100$ m/s, $-50$ m/s, $-20$ m/s, 0 m/s, and $+50$ m/s. Blue dashed line and orange dot-dashed line represent the Rayleigh-Abbe diffraction limit ($0.5\lambda/\mathrm{NA} = 0.525\lambda$) and superoscillation criterion ($0.38\lambda/\mathrm{NA} = 0.399\lambda$), respectively.

has a negligible effect on the focusing effect. This conclusion is reasonable, because the focusing effect is mainly contributed by the waves scattered from the peripheral region of the metalens, which is out of the scope of the background water flow.

In addition, we study the focusing effect of the metalens at different frequencies in Appendix A. We also present another design of the metalens in Appendix B, where a satisfactory focusing effect is achieved with a simpler structure of the meta-atom. In Appendix C we present discussions on the practical realization of a parabolic flow velocity profile and one possible application in practice.

## IV. CONCLUSION

To conclude, we propose a metagrating-based metalens for subdiffraction focusing of waterborne sound. The metalens is composed of a 1D array of iron cylinders embedded in a water background, with each meta-atom consisting of two elliptical cylinders. Based on the grating diffraction theory and intelligent optimization algorithm, each meta-atom is smartly designed so that it deflects a normally incident plane wave exclusively and efficiently along the specified diffraction direction toward the focal spot. In this way, a 3D metalens with a high numerical aperture is constructed by assembling a grating of 32 meta-atoms in the peripheral region and leaving an open space in the central region. Interestingly, a subdiffraction focusing effect breaking the Rayleight-Abbe diffraction limit can be achieved with this simply structured metalens, even after the central region is blocked by a sound-hard sheet. Furthermore, we apply a steady water flow through the central part of the metalens and find that sharp focusing of waterborne sound can still be achieved with free water flow. In addition, the focal depth of the sound wave can be tuned by applying water flows with different flow velocities or opposite flow directions, exhibiting the desired tunability of the focusing functionality. Such sharp and tunable focusing of waterborne sound waves is expected to find applications in fluid-flow-filled scenarios such as in medical imaging and diagnostics, and underwater navigation and communication. The intelligently designed metalens structure may be also used in metagrating-based planar acoustic devices.

## ACKNOWLEDGMENTS

This work is supported by the Guangdong Basic and Applied Basic Research Foundation (Grant No. 2021A1515010322).

## APPENDIX A: FOCUSING EFFECTS AT DIFFERENT FREQUENCIES

In this appendix, we study the focusing effect of the metalens at different frequencies $f$ around the working frequency $f_0 = 200$ kHz, and the results are summarized in Fig. 6. To be more specific, we study the focusing effect in the frequency range from 185 to 210 kHz, in steps of 5 kHz. For those frequencies, the corresponding pressure intensity distributions $|p|^2$ in the longitudinal $x$-$y$ plane and transverse $x$-$z$ plane are plotted in Fig. 6(a). Their focal lengths ($-F_y$) are found to be $-10.37\lambda$, $-12.19\lambda$, $-13.83\lambda$, $-15.33\lambda$, $-17.64\lambda$, and $-19.17\lambda$, respectively. In addition, the intensity profiles along the $y$ axis (i.e., the axis of the metalens) and along the $x$ axis in the focal plane are shown in Figs. 6(b) and 6(c), respectively.

We observe from Figs. 6(a) and 6(b) that the focal length ($F_y$) changes with $f$ (the frequency of the incident wave), exhibiting a dispersive response of the metalens. We also observe a weaker energy concentration effect in the longitudinal direction when $f$ deviates from $f_0$. In comparison, Fig. 6(c) shows that the corresponding FWHMs in the transverse focal plane are $0.424\lambda$, $0.415\lambda$, $0.415\lambda$, $0.409\lambda$, $0.399\lambda$, and $0.407\lambda$, respectively, which means that the resolution in the focal plane is not substantially influenced by the incident wave frequency $f$, exhibiting the desired robustness in terms of the transverse energy concentration effect.

## APPENDIX B: ANOTHER METALENS WITH A RELATIVELY SIMPLE STRUCTURE

In this appendix, we propose another design of the metalens in Fig. 7, where each meta-atom contains two rectangular iron cylinders. When rotating the 2D meta-atoms around the $y$ axis to obtain a full 3D metalens, each rectangular cylinder turns into a ring whose cross-section shape is a rectangle instead of an ellipse, thus being simpler for fabrication. Here we note that in principle we can employ meta-atoms with simpler structures, as long as the

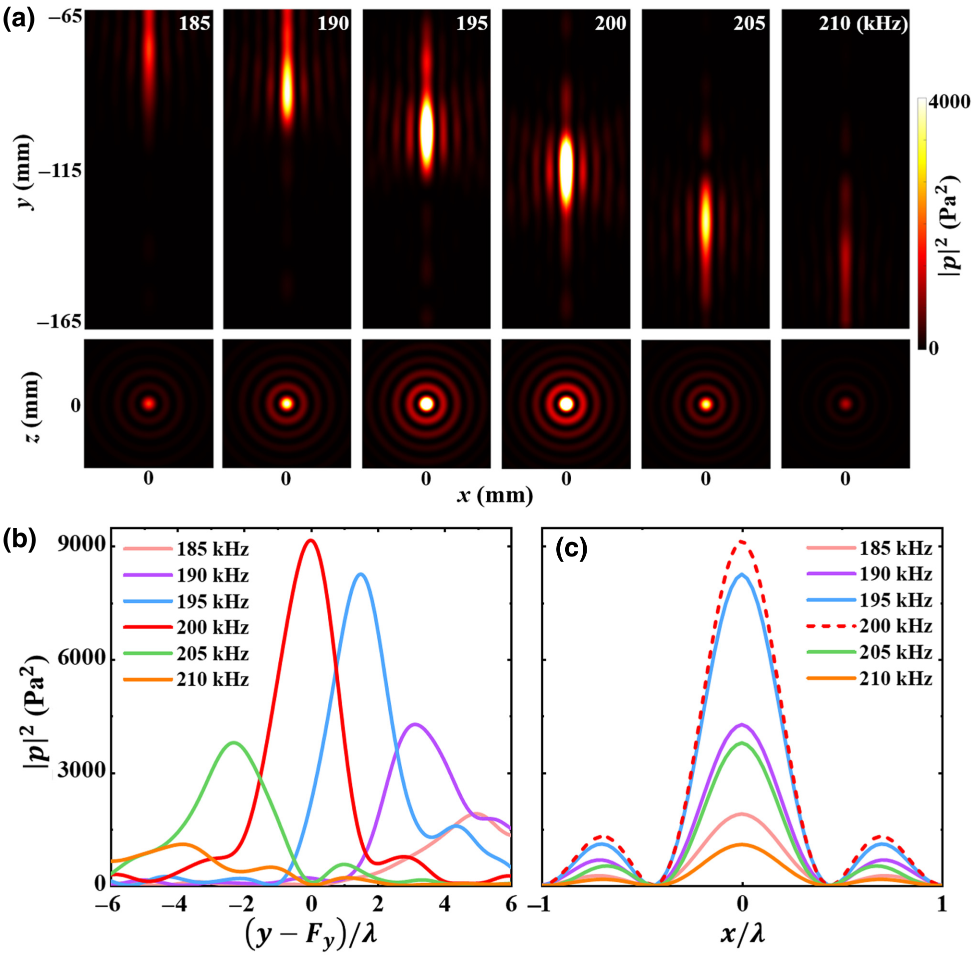

FIG. 6. Focusing effect of the metalens at different frequencies. (a) Intensity field distributions $|p|^2$ in the longitudinal propagation plane and in the transverse focal plane, respectively, for different frequencies. (b),(c) Intensity profiles along the $y$ axis and the $x$ axis of the focal plane, respectively.

geometrical parameters of each meta-atom can provide us enough DOF to simultaneously manipulate the six diffraction orders (three transmitted channels $T_0$, $T_{+1}$, $T_{-1}$, and three reflected channels $R_0$, $R_{+1}$, $R_{-1}$). The two rectangular cylinders have a total of seven DOF including their widths $w_1$ and $w_2$, lengths $h_1$ and $h_2$, and center coordinates $(x_1, 0)$ and $(x_2, y_2)$.

By utilizing the intelligent optimization algorithms, we can obtain the corresponding geometrical parameters of those rectangular cylinders, which are explicitly listed in

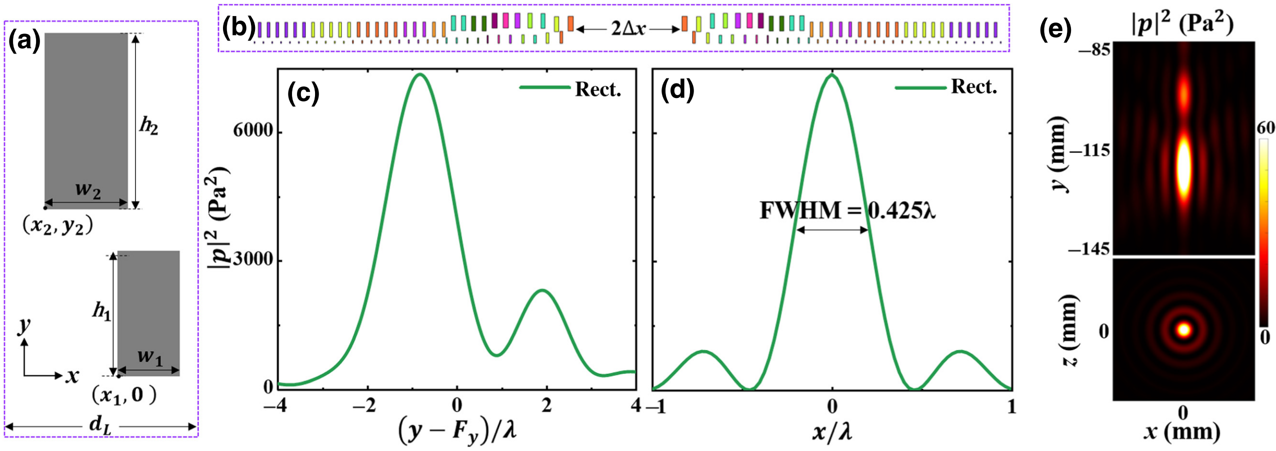

FIG. 7. Another design of the metalens, which has a simpler structure. (a) Schematic of the meta-atom, containing only two rectangular cylinders. (b) 2D cross-section view of the 3D full metalens. (c),(d) Pressure intensity profiles $|p|^2$ along the $y$ axis and the $x$ axis of the focal plane, respectively. (e) $|p|^2$ distributions in the $x$-$y$ plane and $x$-$z$ plane, respectively.

TABLE II. Optimized geometrical parameters of another metalens.

| Unit no. | $L$ | $w_1$ (mm) | $h_1$ (mm) | $w_2$ (mm) | $h_2$ (mm) | $(x_1, y_1)$ (mm) | $(x_2, y_2)$ (mm) |
|---|---|---|---|---|---|---|---|
| 1 | 1 | 2.44 | 10.61 | 4.62 | 13.15 | (11.13, 0) | (1.65, 10.79) |
| 2 | 2 | 2.48 | 9.21 | 3.87 | 13.38 | (9.31, 0) | (0.52, 10.26) |
| 3 | 3 | 2.40 | 7.06 | 3.61 | 13.24 | (8.01, 0) | (0.22, 13.19) |
| 4 | 4 | 2.14 | 7.47 | 3.73 | 13.16 | (7.31, 0) | (0.22, 13.48) |
| 5 | 5 | 1.68 | 7.22 | 4.47 | 13.26 | (7.98, 0) | (0.24, 13.43) |
| 6 | 6 | 1.35 | 7.18 | 4.66 | 13.30 | (8.18, 0) | (0.26, 13.53) |
| 7 | 7 | 1.12 | 6.88 | 4.62 | 13.35 | (8.23, 0) | (0.31, 13.40) |
| 8 | 8, 9 | 1.03 | 4.75 | 3.63 | 13.27 | (7.21, 0) | (0.46, 10.85) |
| 9 | 10, 11 | 1.16 | 4.93 | 3.79 | 13.31 | (7.64, 0) | (0.17, 11.16) |
| 10 | 12, 13 | 0.98 | 3.36 | 2.48 | 13.18 | (6.92, 0) | (0.62, 5.65) |
| 11 | 14 to 16 | 0.93 | 3.12 | 2.45 | 13.15 | (6.69, 0) | (0.66, 5.73) |
| 12 | 17 to 21 | 0.95 | 2.54 | 2.48 | 13.12 | (6.49, 0) | (0.76, 5.63) |
| 13 | 22 to 26 | 0.96 | 1.82 | 2.53 | 13.15 | (6.49, 0) | (0.98, 5.43) |
| 14 | 27 to 32 | 0.88 | 1.47 | 2.46 | 13.20 | (6.49, 0) | (1.12, 5.33) |

Table II. After assembling and rotating all meta-atoms around the $y$ axis, we finally obtain a 3D metalens, whose 2D cross-section view is shown in Fig. 7(b). Let us demonstrate the focusing effect of the metalens under a zero water-flow velocity ($v_0 = 0$ m/s) condition as an example. The pressure intensity field distributions in the longitudinal $x$-$y$ plane and transverse $x$-$z$ plane are shown in Fig. 7(e), where a bright focal spot can be identified. The intensity profiles $|p|^2$ along the $y$ axis and $x$ axis in the focal plane are plotted in Figs. 7(c) and 7(d), respectively. The focus position $(-F_y)$ is found to be $-16.16\lambda$, and the FWHM in the focal plane is $0.425\lambda$, which also breaks the Rayleigh-Abbe diffraction limit.

## APPENDIX C: THE REALIZATION OF A PARABOLIC VELOCITY PROFILE AND A POSSIBLE APPLICATION

In this appendix we firstly show that a water flow with a parabolic velocity profile can be easily generated and then utilized for the central region of the metalens.

The simplest example is the Poiseuille flow in a straight tube, which shows a parabolic distribution of velocity. By equating the viscous force with the pressure gradient force in the water flow, and requiring the boundary condition of $v = 0$ at $r = R$ (where $R$ is the radius of the tube), we can obtain the following velocity profile:

$$v = v_0\left(1 - \frac{r^2}{R^2}\right). \tag{C1}$$

Equation (C1) unambiguously indicates that the water flow velocity $v$ has a parabolic profile inside the tube, and is exactly the same as Eq. (3) of the main text. The derivation of Eq. (C1) can be found in many textbooks on fluid mechanics, e.g., Ref. [50].

Thus, it is straightforward to realize such a parabolic water-flow field in the experiment. As shown in Fig. 8, we firstly introduce a uniform water flow at the inlet of the tube. Then, at a place far away from the inlet, the water flow gradually evolves into a Poiseuille flow with a parabolic velocity profile. By leading such a Poiseuille

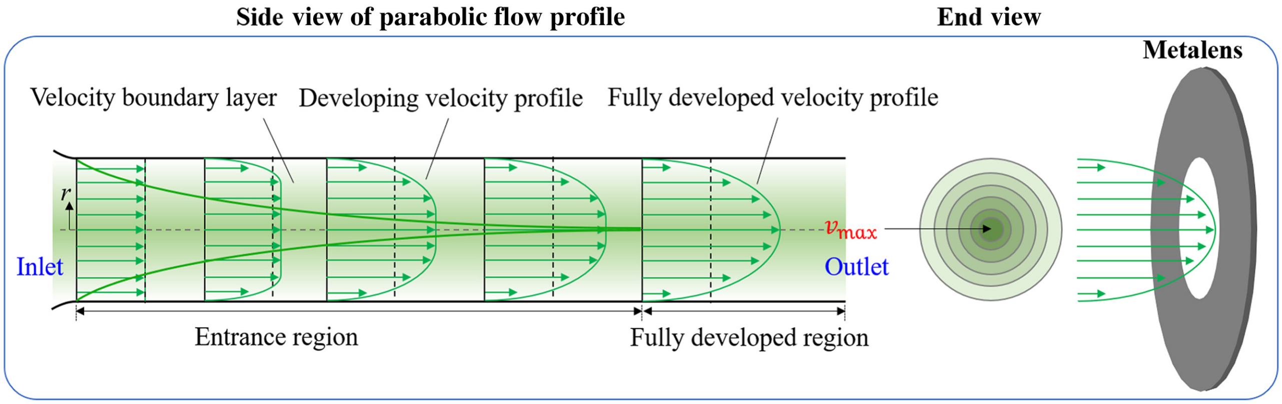

FIG. 8. Schematic diagram of a proposed experimental setup.

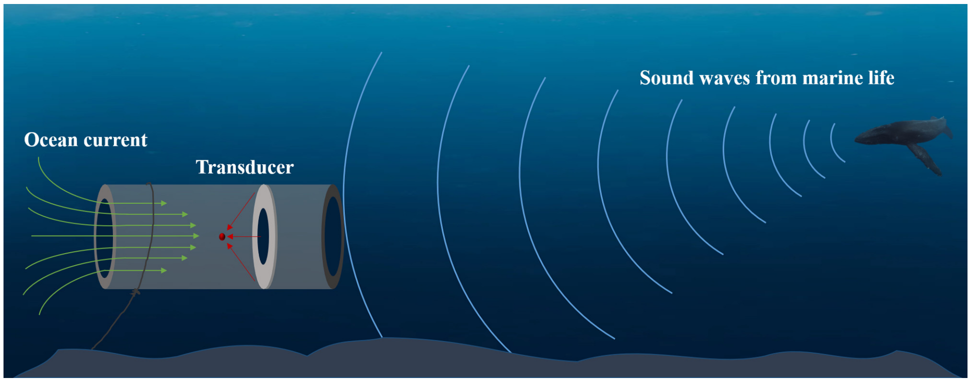

FIG. 9. Application of the metalens in a sonar system for the detection of marine life.

flow into the central region of the metalens, as shown in Fig. 8, we can study the focusing effect of the metalens.

Next, we discuss how a flow in the central region can be exploited in practice. To be more specific, we show that the metalens proposed in this work could be integrated into a sonar system for the detection of deep-sea marine life. In this regard, one conventional method involves the use of a floating sonar system fixed around the seabed, which can detect nearby marine life when the acoustic signal (either produced or scattered by the marine life) is collected by the transducer in the sonar. Such a conventional sonar system can be improved by integrating the metalens into the system. As shown schematically in Fig. 9, we could design a hollow-tube sonar system with an integrated metalens, which has the following advantages. Firstly, the metalens with a huge energy concentration ratio and subdiffraction resolution can greatly enhance the sensitivity of the sonar system, so that even a very feeble acoustic signal can be detected and identified. Secondly, there are always ocean currents flowing around the sonar system, which generate a persisting flow resistance for a conventional sonar system. In contrast, a hollow-tube sonar system permits water flow through its central region, thus greatly reducing flow resistance and increasing the lifetime of the sonar system. Furthermore, superresolution focusing of the acoustic signal can be achieved even in the presence of an ocean flow, which substantially benefits practical application. To summarize, a water flow in the central region of the metalens can be exploited in the sonar system for the detection of deep-sea marine life.

[1] W. T. Chen, A. Y. Zhu, V. Sanjeev, M. Khorasaninejad, Z. Shi, E. Lee, and F. Capasso, A broadband achromatic metalens for focusing and imaging in the visible, Nat. Nanotechnol. **13**, 220 (2018).

[2] S. Wang, P. C. Wu, V. C. Su, Y. C. Lai, M. K. Chen, H. Y. Kuo, B. H. Chen, Y. H. Chen, T. T. Huang, J. H. Wang, *et al.*, A broadband achromatic metalens in the visible, Nat. Nanotechnol. **13**, 227 (2018).

[3] C. Liu, J. Shi, W. Zhao, X. Zhou, C. Ma, R. Peng, M. Wang, Z. H. Hang, X. Liu, J. Christensen, *et al.*, Three-Dimensional Soundproof Acoustic Metacage, Phys. Rev. Lett. **127**, 084301 (2021).

[4] R. Dong, M. Sun, F. Mo, D. Mao, X. Wang, and Y. Li, Recent advances in acoustic ventilation barriers, J. Phys. D: Appl. Phys. **54**, 403002 (2021).

[5] L. Shen, Y. Zhu, F. Mao, S. Gao, Z. Su, Z. Luo, H. Zhang, and B. Assouar, Broadband Low-Frequency Acoustic Metamuffler, Phys. Rev. Appl. **16**, 064057 (2021).

[6] H. Long, C. Shao, Y. Cheng, J. Tao, and X. Liu, High absorption asymmetry enabled by a deep-subwavelength ventilated sound absorber, Appl. Phys. Lett. **118**, 263502 (2021).

[7] R. Dong, D. Mao, Y. Zhu, F. Mo, X. Wang, and Y. Li, A ventilating acoustic barrier for attenuating broadband diffuse sound, Appl. Phys. Lett. **119**, 263505 (2021).

[8] J. He, Z. Zhou, C. Zhang, Y. Zheng, Y. Li, Y. Li, X. Jiang, and D. Ta, Ultrasparse and omnidirectional acoustic ventilated meta-barrier, Appl. Phys. Lett. **120**, 191701 (2022).

[9] N. Yu, P. Genevet, M. A. Kats, F. Aieta, J. Tetienne, F. Capasso, and Z. Gaburro, Light propagation with phase discontinuities: Generalized laws of reflection and refraction, Science **334**, 333 (2011).

[10] A. Díaz-Rubio and S. A. Tretyakov, Acoustic metasurfaces for scattering-free anomalous reflection and refraction, Phys. Rev. B **96**, 125409 (2017).

[11] B. Assouar, B. Liang, Y. Wu, Y. Li, J. C. Cheng, and Y. Jing, Acoustic metasurfaces, Nat. Rev. Mater. **3**, 460 (2018).

[12] Y. Li, B. Liang, X.-Y. Zou, and J. C. Cheng, Extraordinary acoustic transmission through ultrathin acoustic metamaterials by coiling up space, Appl. Phys. Lett. **103**, 063509 (2013).

[13] J. Zhao, B. Li, Z. N. Chen, and C. W. Qiu, Redirection of sound waves using acoustic metasurface, Appl. Phys. Lett. **103**, 151604 (2013).

[14] J. Mei and Y. Wu, Controllable transmission and total reflection through an impedance-matched acoustic metasurface, New J. Phys. **16**, 123007 (2014).

[15] Y. Cheng, C. Zhou, B. G. Yuan, D. J. Wu, Q. Wei, and X. J. Liu, Ultra-sparse metasurface for high reflection of low-frequency sound based on artificial Mie resonances, Nat. Mater. **14**, 1013 (2015).

[16] J. Li, C. Shen, A. Díaz-Rubio, S. A. Tretyakov, and S. A. Cummer, Systematic design and experimental demonstration of bianisotropic metasurfaces for scattering-free manipulation of acoustic wavefronts, Nat. Commun. **9**, 1342 (2018).

[17] J. Mei, G. Ma, M. Yang, Z. Yang, W. Wen, and P. Sheng, Dark acoustic metamaterials as super absorbers for low-frequency sound, Nat. Commun. **3**, 756 (2012).

[18] G. Ma, M. Yang, S. Xiao, Z. Yang, and P. Sheng, Acoustic metasurface with hybrid resonances, Nat. Mater. **13**, 873 (2014).

[19] J. Mei, X. Zhang, and Y. Wu, Ultrathin metasurface with high absorptance for waterborne sound, J. Appl. Phys. **123**, 091710 (2018).

[20] Y. Li and B. M. Assouar, Acoustic metasurface-based perfect absorber with deep subwavelength thickness, Appl. Phys. Lett. **108**, 063502 (2016).

[21] X. Jiang, Y. Li, D. Ta, and W. Wang, Ultrasonic sharp autofocusing with acoustic metasurface, Phys. Rev. B **102**, 064308 (2020).

[22] H. T. Zhou, W. X. Fu, Y. F. Wang, and Y. S. Wang, High-Efficiency Ultrathin Nonlocal Waterborne Acoustic Metasurface, Phys. Rev. Appl. **15**, 044046 (2021).

[23] Y. Ra Di, D. L. Sounas, and A. Alù, Metagratings: Beyond the Limits of Graded Metasurfaces for Wave Front Control, Phys. Rev. Lett. **119**, 067404 (2017).

[24] D. Torrent, Acoustic anomalous reflectors based on diffraction grating engineering, Phys. Rev. B **98**, 060101 (2018).

[25] Y. Fu, C. Shen, Y. Cao, L. Gao, H. Chen, C. T. Chan, S. A. Cummer, and Y. Xu, Reversal of transmission and reflection based on acoustic metagratings with integer parity design, Nat. Commun. **10**, 2326 (2019).

[26] Y. Yang, H. Jia, Y. Bi, H. Zhao, and J. Yang, Experimental Demonstration of an Acoustic Asymmetric Diffraction Grating Based on Passive Parity-Time-Symmetric Medium, Phys. Rev. Appl. **12**, 034040 (2019).

[27] L. Fan and J. Mei, Metagratings for Waterborne Sound: Various Functionalities Enabled by an Efficient Inverse Design Approach, Phys. Rev. Appl. **14**, 044003 (2020).

[28] Y. K. Chiang, S. Oberst, A. Melnikov, L. Quan, S. Marburg, A. Alù, and D. A. Powell, Reconfigurable Acoustic Metagrating for High-Efficiency Anomalous Reflection, Phys. Rev. Appl. **13**, 064067 (2020).

[29] Z. Du and J. Mei, Metagrating-based acoustic wavelength division multiplexing enabled by deterministic and probabilistic deep learning models, Phys. Rev. Res. **4**, 033165 (2022).

[30] L. Fan and J. Mei, Acoustic Metagrating Circulators: Nonreciprocal, Robust, and Tunable Manipulation with Unitary Efficiency, Phys. Rev. Appl. **15**, 064002 (2021).

[31] L. Fan and J. Mei, Multifunctional Waterborne Acoustic Metagratings: From Extraordinary Transmission to Total and Abnormal Reflection, Phys. Rev. Appl. **16**, 044029 (2021).

[32] J. He, X. Jiang, D. Ta, and W. Wang, Experimental demonstration of underwater ultrasound cloaking based on metagrating, Appl. Phys. Lett. **117**, 091901 (2020).

[33] Y. Fu, C. Shen, X. Zhu, J. Li, Y. Liu, S. Cummer, and Y. Xu, Sound vortex diffraction via topological charge in phase gradient metagratings, Sci. Adv. **6**, eaba9876 (2020).

[34] J. Mei, L. Fan, and X. Hong, Elastic Metagratings with Simultaneous Highly Efficient Control over Longitudinal and Transverse Waves for Multiple Functionalities, Phys. Rev. Appl. **18**, 014002 (2022).

[35] J. Mei, L. Fan, and X. Hong, Elastic metagratings with simultaneous modulation of reflected and transmitted waves, Crystals **12**, 901 (2022).

[36] Y. K. Chiang, L. Quan, Y. Peng, S. Sepehrirahnama, S. Oberst, A. Alù, and D. A. Powell, Scalable Metagrating for Efficient Ultrasonic Focusing, Phys. Rev. Appl. **16**, 064014 (2021).

[37] J. Qian, J. P. Xia, H. X. Sun, Y. Wang, Y. Ge, S. Q. Yuan, Y. Yang, X. J. Liu, and B. Zhang, Aperiodic metagratings for high-performance multifunctional acoustic lenses, Adv. Mater. Technol. **5**, 2000542 (2020).

[38] Y. J. Lu, H. Y. Zou, J. Qian, Y. Wang, Y. Ge, S. Q. Yuan, H. X. Sun, and X. J. Liu, Multifunctional reflected lenses based on aperiodic acoustic metagratings, Appl. Phys. Lett. **119**, 173501 (2021).

[39] J. Mei, L. Fan, and X. B. Hong, Broadband and high-numerical-aperture sharp focusing for waterborne sound with metagrating-based lens, New J. Phys. **24**, 093014 (2022).

[40] M. Kang, Y. Ra'di, D. Farfan, and A. Alù, Efficient Focusing with Large Numerical Aperture Using a Hybrid Metalens, Phys. Rev. Appl. **13**, 044016 (2020).

[41] G. Chen, Z. Q. Wen, and C. W. Qiu, Superoscillation: From physics to optical applications, Light: Sci. Appl. **8**, 56 (2019).

[42] N. I. Zheludev and G. Yuan, Optical superoscillation technologies beyond the diffraction limit, Nat. Rev. Phys. **4**, 16 (2022).

[43] G. Gbur, Using superoscillations for superresolved imaging and subwavelength focusing, Nanophotonics **8**, 205 (2019).

[44] F. M. Huang and N. I. Zheludev, Super-resolution without evanescent waves, Nano Lett. **9**, 1249 (2009).

[45] F. M. Huang, Y. Chen, F. J. G. de Abajo, and N. I. Zheludev, Optical super-resolution through super-oscillations, J. Opt. A: Pure Appl. Opt. **9**, S285 (2007).

[46] K. Huang, H. Ye, J. Teng, S. P. Yeo, B. Luk'yanchuk, and C. W. Qiu, Optimization-free superoscillatory lens using phase and amplitude masks, Laser Photonics Rev. **8**, 152 (2014).

[47] F. Zhao, Z. Li, X. Dai, X. Liao, S. Li, J. Cao, Z. Shang, Z. Zhang, G. Liang, G. Chen, *et al.*, Broadband achromatic sub-diffraction focusing by an amplitude-modulated terahertz metalens, Adv. Opt. Mater. **8**, 2000842 (2020).

[48] Y. X. Shen, Y. G. Peng, F. Cai, K. Huang, D. G. Zhao, C. W. Qiu, H. Zheng, and X. F. Zhu, Ultrasonic super-oscillation wave-packets with an acoustic meta-lens, Nat. Commun. **10**, 3411 (2019).

[49] Z. Wen, Y. He, Y. Li, L. Chen, and G. Chen, Superoscillation focusing lens based on continuous amplitude and binary phase modulation, Opt. Express **22**, 22163 (2014).

[50] *Chapter 2, Fluid Mechanics*, 2nd ed., edited by L. D. Landau, E. M. Lifshitz (Pergamon, Oxford, 1987), pp. 44–94.